AMERICAN SOCIETY FOR MICROBIOLOGY | mBio®

RESEARCH ARTICLE
Host-Microbe Biology

Zn^{2+} Intoxication of *Mycobacterium marinum* during *Dictyostelium discoideum* Infection Is Counteracted by Induction of the Pathogen Zn^{2+} Exporter CtpC

Nabil Hanna,[a] Hendrik Koliwer-Brandl,[b] Louise H. Lefrançois,[a] Vera Kalinina,[a]* Elena Cardenal-Muñoz,[a] Joddy Appiah,[a] Florence Leuba,[a] Aurélie Gueho,[a]* Hubert Hilbi,[b] Thierry Soldati,[a] Caroline Barisch[a]*

[a]Department of Biochemistry, Faculty of Science, University of Geneva, Geneva, Switzerland
[b]Institute of Medical Microbiology, University of Zurich, Zurich, Switzerland

Thierry Soldati and Caroline Barisch contributed equally.

ABSTRACT Macrophages use diverse strategies to restrict intracellular pathogens, including either depriving the bacteria of (micro)nutrients such as transition metals or intoxicating them via metal accumulation. Little is known about the chemical warfare between *Mycobacterium marinum*, a close relative of *Mycobacterium tuberculosis* (Mtb), and its hosts. We use the professional phagocyte *Dictyostelium discoideum* to investigate the role of Zn^{2+} during *M. marinum* infection. We show that *M. marinum* senses toxic levels of Zn^{2+} and responds by upregulating one of its isoforms of the Zn^{2+} efflux transporter CtpC. Deletion of *ctpC* (MMAR_1271) leads to growth inhibition in broth supplemented with Zn^{2+} as well as reduced intracellular growth. Both phenotypes were fully rescued by constitutive ectopic expression of the Mtb CtpC orthologue demonstrating that MMAR_1271 is the functional CtpC Zn^{2+} efflux transporter in *M. marinum*. Infection leads to the accumulation of Zn^{2+} inside the *Mycobacterium*-containing vacuole (MCV), achieved by the induction and recruitment of the *D. discoideum* Zn^{2+} efflux pumps ZntA and ZntB. In cells lacking ZntA, there is further attenuation of *M. marinum* growth, presumably due to a compensatory efflux of Zn^{2+} into the MCV, carried out by ZntB, the main Zn^{2+} transporter in endosomes and phagosomes. Counterintuitively, bacterial growth is also impaired in *zntB* KO cells, in which MCVs appear to accumulate less Zn^{2+} than in wild-type cells, suggesting restriction by other Zn^{2+}-mediated mechanisms. Absence of CtpC further epistatically attenuates the intracellular proliferation of *M. marinum* in *zntA* and *zntB* KO cells, confirming that mycobacteria face noxious levels of Zn^{2+}.

IMPORTANCE Microelements are essential for the function of the innate immune system. A deficiency in zinc or copper results in an increased susceptibility to bacterial infections. Zn^{2+} serves as an important catalytic and structural cofactor for a variety of enzymes including transcription factors and enzymes involved in cell signaling. But Zn^{2+} is toxic at high concentrations and represents a cell-autonomous immunity strategy that ensures killing of intracellular bacteria in a process called zinc poisoning. The cytosolic and lumenal Zn^{2+} concentrations result from the balance of import into the cytosol via ZIP influx transporters and efflux via ZnT transporters. Here, we show that Zn^{2+} poisoning is involved in restricting *Mycobacterium marinum* infections. Our study extends observations during *Mycobacterium tuberculosis* infection and explores for the first time how the interplay of ZnT transporters affects mycobacterial infection by impacting Zn^{2+} homeostasis.

KEYWORDS *Dictyostelium discoideum*, *Mycobacterium marinum*, infection, zinc poisoning, zinc transporters, ZnTs, CtpC

Citation Hanna N, Koliwer-Brandl H, Lefrançois LH, Kalinina V, Cardenal-Muñoz E, Appiah J, Leuba F, Gueho A, Hilbi H, Soldati T, Barisch C. 2021. Zn^{2+} intoxication of *Mycobacterium marinum* during *Dictyostelium discoideum* infection is counteracted by induction of the pathogen Zn^{2+} exporter CtpC. mBio 12:e01313-20. https://doi.org/10.1128/mBio.01313-20.

Editor Carmen Buchrieser, Institut Pasteur

Copyright © 2021 Hanna et al. This is an open-access article distributed under the terms of the Creative Commons Attribution 4.0 International license.

Address correspondence to Thierry Soldati, thierry.soldati@unige.ch, or Caroline Barisch, caroline.barisch@uos.de.

* Present address: Vera Kalinina, Institute of Cytology, Russian Academy of Sciences, St. Petersburg, Russia; Aurélie Gueho, Protim, Université de Rennes, Rennes, France; Caroline Barisch, Division of Molecular Infection Biology, Department of Biology/Chemistry, University of Osnabrück, Osnabrück, Germany.

Received 20 May 2020
Accepted 4 December 2020
Published 2 February 2021

Mycobacterium marinum is a pathogen that causes a tuberculosis-like infection in fish and amphibians, in which it generates granulomas very similar to those caused in humans by its close relative *Mycobacterium tuberculosis* (Mtb). *M. marinum* also opportunistically infects humans, but these infections are limited to the skin and extremities due to their lower temperature (1). At the level of the host macrophage, the course of infection by both *M. marinum* and Mtb is strikingly similar, making *M. marinum* an experimentally versatile model to study pathogenic mechanisms of tuberculosis (2). Apart from fish and mammalian phagocytes, another model host for *M. marinum* is the soil amoeba *Dictyostelium discoideum* (3), the endocytic and cell-autonomous defense pathways of which are well conserved with humans (4).

Upon phagocytic uptake, *M. marinum* resides inside a phagosome that is actively modified by the bacterium to rapidly divert from the canonical maturation pathway, to become a replicative niche, the so-called *Mycobacterium*-containing vacuole (MCV). Like Mtb, *M. marinum* was thought to be a vacuolar pathogen. However, accumulating evidence indicates that both bacteria also reside and proliferate in the cytosol, where access to nutrients is not limited but bacteria are exposed to cytosolic defenses (3, 5, 6). *M. marinum* starts damaging the MCV in the first hours of infection, before full rupture of the compartment releases the bacteria into the host cytosol at around 24 to 36 h. As also shown for Mtb, perforation of the MCV and escape to the cytosol are achieved, among other means, by secretion of the membrane-damaging peptide ESAT-6 through the mycobacterial ESX-1 type VII secretion system (T7SS) (3, 7–13).

Infected cells use a vast repertoire of strategies to fight intracellular mycobacteria. For instance, *M. marinum* infection has been shown to induce inducible nitric oxide synthase (iNOS) gene expression in fish macrophages (14), and neutrophils kill these bacilli through reactive oxygen species (ROS)-dependent mechanisms (15). In addition, *M. marinum* is targeted for digestion by the autophagy machinery of murine macrophages (16) and *D. discoideum* (3, 8). However, these mycobacteria have also evolved mechanisms of counterdefense against their hosts. They downregulate iNOS levels (17) and suppress the production of reactive nitrogen intermediates, decrease the expression of NADPH oxidase components, and reduce the production of ROS (14). Moreover, *M. marinum* avoids phagosome maturation by (i) modulating the composition of its cell wall (18) or the MCV content in phosphatidylinositol-3-phosphate (PtdIns3*P* [19]), (ii) impairing the recruitment of the endosomal sorting complex required for transport (ESCRT)-0 component Hrs (20), and (iii) avoiding accumulation of lysosomal enzymes (3, 16, 19, 21, 22). It also blocks the autophagic flux, which would eventually deliver the bacteria into autolysosomes for killing (3, 16).

Apart from the defense mechanisms mentioned above, little is known about the chemical warfare between *M. marinum* and its hosts, and especially about the manipulation of transition metals. In the case of Mtb, immune cells deprive the bacteria of essential nutrients such as iron and manganese, while they intoxicate the mycobacteria by accumulating copper and zinc inside the MCV (23–26). However, Mtb resists this metal-centered fight with an arsenal of metal-binding proteins, oxidases, and efflux transporters. For instance, Mtb captures Fe^{3+} from macrophages through its siderophore mycobactin (27), but it keeps low intracellular Cu^{2+} levels with its CtpV and MctB transporters and the Cu^{2+}-binding metallothionein MymT (24, 28, 29). Mtb also resists the toxic free Zn^{2+} burst induced in human macrophages by exporting Zn^{2+} through the P-type ATPase CtpC (30), an efflux pump also present in two isoforms in *M. marinum* (31). On the host side, the mRNA levels of various Zn^{2+} transporters (i.e., ZIP8, ZnT1, ZIP1, and ZIP10) are altered in fish granulomas compared to resting macrophages (32). However, little is known about the conservation of these host-versus-pathogen strategies, and especially how the two mycobacterial CtpC and host Zn^{2+} transporters impact *M. marinum* infection in *D. discoideum*.

D. discoideum possesses four Zn^{2+} efflux transporters of the ZnT family (Znts) and

11 Zn^{2+} influx transporters of the ZIP family (Zpls). ZntA locates to the contractile vacuole (CV), an organelle that regulates the osmotic and metal balances in the cell, and ZntB to organelles of the endosomal pathway (33, 34). While ZntA does not have any close homologue, ZntB shares homology with human ZNT1 and ZNT10, the latter being also present at early endosomes (4). Similarly to their human homologs ZNT6 and ZNT7, located in the early secretory pathway (4), *D. discoideum* ZntC and ZntD localize to the Golgi complex or recycling endosomes (33). We wondered whether these ZnTs were part of the host defense mechanisms against *M. marinum* infection. We demonstrate here that *D. discoideum* intoxicates *M. marinum* by inducing the expression and recruitment of ZntA and ZntB, but not ZntC nor ZntD, to the MCV. However, *M. marinum* resists the *D. discoideum* Zn^{2+} immune response by specifically expressing its Zn^{2+} exporter CtpC.

RESULTS

Free Zn^{2+} accumulates within intact *M. marinum*-containing vacuoles. In *D. discoideum*, free Zn^{2+} accumulates inside (i) the CV network, (ii) zincosomes (endosomal compartments with lysosomal and postlysosomal characteristics), and (iii) phagosomes containing beads and nonpathogenic bacteria such as *Escherichia coli* or *Mycobacterium smegmatis* (33, 35) (summarizing scheme is in Fig. 1A). We wondered whether vacuoles containing the pathogenic bacterium *M. marinum* or *M. marinum* ΔRD1, a mutant lacking a functional ESX-1 secretion system and thus strongly attenuated in inducing membrane damage and escaping to the cytosol (8, 9), also accumulate Zn^{2+}. We monitored infected cells expressing the endosomal and MCV marker AmtA-mCherry (36) and labeled with the pH-independent Zn^{2+} probe NBD-TPEA (33) (Fig. 1B). Intact MCVs of the ΔRD1 mutant accumulated Zn^{2+} at all the stages of infection (Fig. 1B and C). In contrast, numerous compartments of *M. marinum* wild type (wt) appeared devoid of Zn^{2+}, likely because it leaked out of either subtly or visibly broken MCVs (Fig. 1B). Quantification of NBD-TPEA-labeled MCVs confirmed that, because damage increases as infection progresses, fewer and fewer compartments containing wt bacteria were positive for Zn^{2+} (Fig. 1C).

***M. marinum* senses and reacts to toxic levels of Zn^{2+} by inducing its CtpC Zn^{2+} efflux pump.** During infection of macrophages, Mtb is exposed to a burst of transition metals that induces the expression of efflux P-type ATPases such as CtpC, CtpG, and CtpV (30, 37). In particular, CtpC expression helps Mtb detoxify excess Zn^{2+}, which the host transports inside the MCV (30). The expression of Mtb *ctpV* is also induced during macrophage infection (28), which is essential for virulence and survival in response to elevated copper levels in the MCV (28). The genome of *M. marinum* encodes 20 P-type ATPases that are phylogenetically close to their Mtb homologues (see Fig. S1 in the supplemental material). Interestingly, *M. marinum* has two homologues of CtpC, CtpC (MMAR_1271) and CtpC-like (MMAR_2147). Inspection of our parallel RNA-sequencing (RNA-Seq) results of *M. marinum* and *D. discoideum* during infection (38) revealed that, as shown for Mtb, expression of the *ctpC* gene increased at all time points and reached its maximum 36 h postinfection (hpi) compared to *M. marinum* grown in broth (Fig. 2A, Fig. S2, and Table S1A). Expression of the *ctpc*-like gene was increased only later during infection and also peaked at 36 hpi (Fig. 2A, Fig. S2, and Table S1A). These results suggest a possible specific role of the two CtpC P-type ATPases in the detoxification of Zn^{2+} during infection. It is noteworthy that other P-type ATPases were differentially expressed during infection, including the three *M. marinum* CtpV homologues, suggesting a complex scenario in which *M. marinum* faces elevated levels of other ions (Fig. S2 and Table S1A).

We next attempted to evaluate whether the expression of *ctpC* is influenced by Zn^{2+}. To this end, the expression levels of selected P-type ATPases were determined by qRT-PCR analysis. Supplementing the growth medium with increasing concentration of $ZnSO_4$ strongly enhanced the transcription of *ctpC* but not *ctpC*-like, *ctpV*, or *ctpV*-like (Fig. 2B). These results suggest that CtpC is exclusively involved in detoxification of Zn^{2+} in *M. marinum* and that CtpC-like might function under different circumstances than those tested.

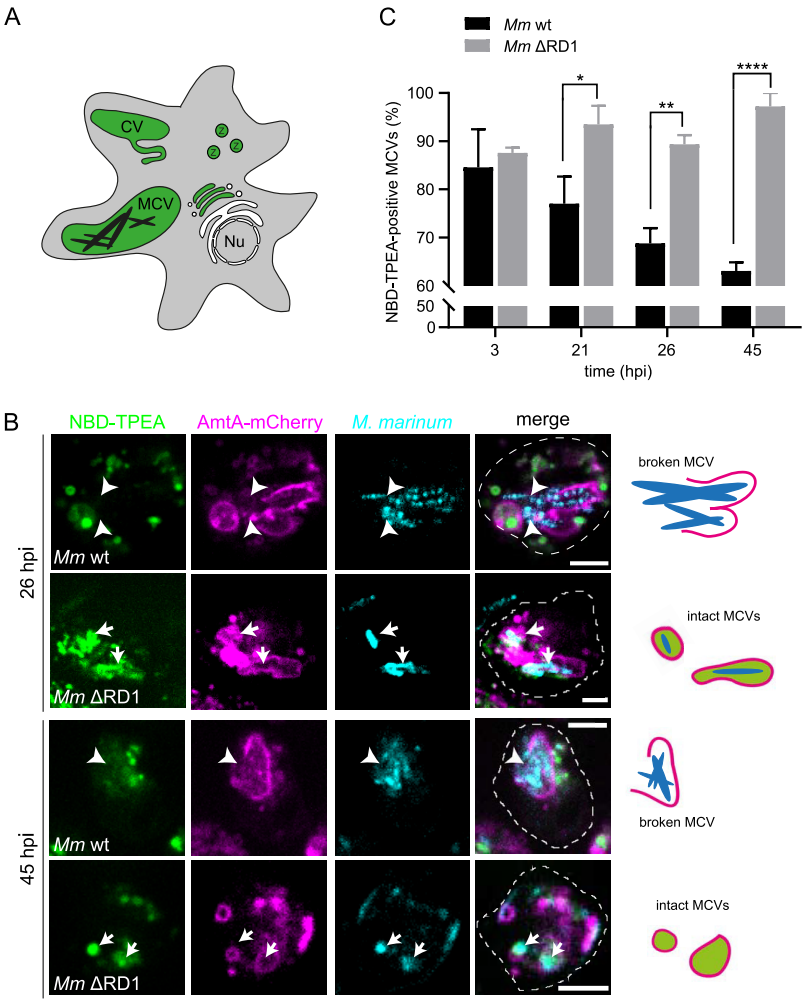

FIG 1 Free Zn^{2+} accumulates inside the MCV. (A) Scheme depicting the different localizations of free Zn^{2+} in *D. discoideum*: zincosomes (Z), contractile vacuole (CV), and phagosomes (e.g., MCVs [33]). Nu, nucleus. (B) Live cell imaging and illustrations of NBD-TPEA-treated cells expressing AmtA-mCherry (magenta). *M. marinum* was stained with Vybrant DyeCycle Ruby (cyan) before imaging. Arrows point at Zn^{2+}-positive MCVs; arrowheads label bacteria exposed to the *D. discoideum* cytosol. Scale bars, 5 μm. One example is shown for wt and ΔRD1 *M. marinum* at 26 and 45 hpi, respectively. The cartoons illustrate the heterogeneity of Zn^{2+} labeling in intact and broken MCVs. (C) Percentage of NBD-TPEA-positive MCVs at different times post-infection with *M. marinum* wt and ΔRD1. Bars represent the mean and SEM from three independent experiments. About 300 wt and 200 ΔRD1 MCVs were counted in total. Statistical differences were calculated with a Fisher least significant difference (LSD) *post hoc* test after two-way ANOVA (*, $P < 0.05$; **, $P < 0.01$; ****, $P < 0.0001$).

To investigate the physiological role of CtpC, we constructed a deletion mutant of *ctpC* (MMAR_1271; Fig. 2B). *M. marinum* wt and its isogenic mutant Δ*ctpC* grew similarly in broth and on agar, indicating no constitutive growth defect (Fig. S3A and E to G). However, the growth of *M. marinum* Δ*ctpC* in broth was impaired in the presence of Zn^{2+} in a dose-dependent manner (Fig. 2C and Fig. S3B to E). In addition, its growth was impaired on solid medium containing elevated levels of Zn^{2+} but not of Mn^{2+} or Cu^{2+} (Fig. S3E to G), demonstrating that the absence of *ctpC* renders *M. marinum* specifically susceptible to Zn^{2+}. Strikingly, the intracellular growth of *M. marinum* Δ*ctpC* was notably impaired (Fig. 2D). Most importantly, both the growth defect of Δ*ctpC* in broth supplemented with Zn^{2+} (Fig. 2C) and the intracellular growth (Fig. 2D) were fully rescued by constitutive expression of the Mtb CtpC orthologue (Rv3270). Together, these results demonstrate that the susceptibility of *M. marinum* Δ*ctpC* to Zn^{2+} is solely due to the lack of CtpC and that MMAR_1271 is the functional

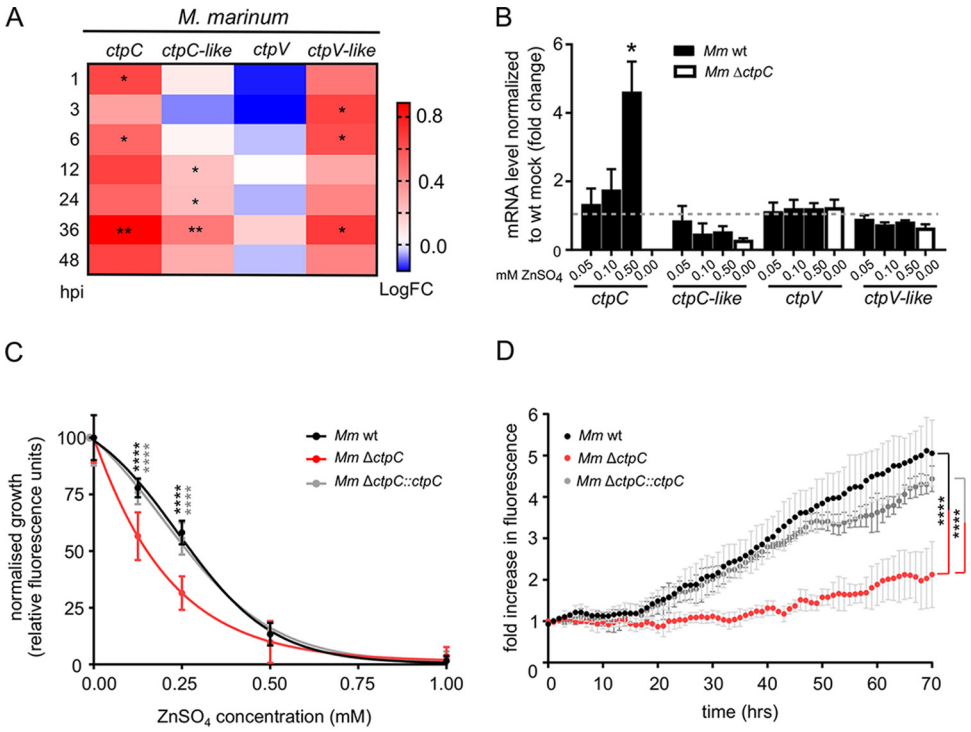

FIG 2 *M. marinum* senses and reacts to toxic levels of Zn^{2+} during infection and *in vitro*. (A) Heat map representing the transcriptional data shown in Table S1A. Cells were infected with GFP-expressing *M. marinum* wt, and samples were collected at different hpi. The time points with statistically significant differential expression are marked with asterisks (*, $P < 0.05$; **, $P < 0.01$). Colors indicate the amplitude of expression of *M. marinum ctpC*, *ctpC*-like, *ctpV*, and *ctpV*-like (in logarithmic fold change [logFC]) in infected cells compared to *M. marinum* grown in broth: from dark red (highest expression) to dark blue (lowest expression). (B) Normalized mRNA levels of *Mm_ctpC*, *Mm_ctpC*-like, *Mm_ctpV*, and *Mm_CtpV*-like in GFP-expressing *M. marinum* grown in 7H9 with increasing concentrations of $ZnSO_4$ compared to bacteria grown in 7H9 without extra $ZnSO_4$ (depicted as dashed gray line). To confirm the successful deletion of *ctpC*, the mRNA levels in *M. marinum* Δ*ctpC* were tested as well. Shown are mean and standard deviations from two independent experiments. Statistical differences were calculated with an unpaired *t* test (*, $P < 0.05$). (C) Dose-response curves of *M. marinum* wt, Δ*ctpC*, and Δ*ctpC*::*ctpC* grown in broth supplemented with increasing concentrations of $ZnSO_4$ (0, 0.125, 0.25, 0.5, and 1 mM). The fluorescence intensities of GFP and E2-Crimson were used as a proxy for bacterial growth. The areas under the curve were calculated for the three strains, and the values were plotted as a function of $ZnSO_4$ concentrations. Error bars indicate the SD from eight technical replicates from two independent biological replicates. Statistical differences were calculated with a Fisher LSD test after two-way ANOVA (****, $P < 0.0001$). (D) *D. discoideum* was infected with GFP- or E2-Crimson-expressing *M. marinum* wt, Δ*ctpC* (GFP expressing), or Δ*ctpC*::*ctpC* (E2-Crimson expressing). The intracellular bacterial growth (in relative fluorescence units [RFUs]) was monitored every hour. Shown is the fold increase in bacterial fluorescence over time of two independent biological replicates. Error bars indicate the SD from eight technical replicates. Statistical differences were calculated with Dunnett's multiple-comparison test after two-way ANOVA (****, $P < 0.0001$).

orthologue of Mtb CtpC. We conclude that, during infection of *D. discoideum*, *M. marinum* is exposed to toxic concentrations of Zn^{2+} and that the bacteria counteract this intoxication by specifically inducing the Zn^{2+} efflux pump CtpC.

The *D. discoideum* Zn^{2+} transporters ZntA and ZntB localize to the *M. marinum* MCV. We wondered which of the four *D. discoideum* Zn^{2+} efflux transporters ZntA, ZntB, ZntC, and ZntD (33) localized to the MCV and led to Zn^{2+} accumulation. To ensure optimal preservation of membranes and organelles including the MCV and CV for immunofluorescence, we performed fixation/permeabilization in ultracold methanol (39, 40). Only ZntA and ZntB (Fig. 3A and B), but neither ZntC nor ZntD (Fig. S4A and B), localized to the MCV. While 20% of the MCVs were positive for ZntA (Fig. 3C), ZntB was present at around 50 to 60% of the MCVs throughout the infection cycle (Fig. 3D). Because ZntA is localized exclusively at the CV membrane in noninfected cells (33), we confirmed its localization at the MCV by live imaging. Strikingly, besides ZntA (Fig. S4C) other CV resident proteins such as Rab11a and Rab11c (41) were present at the MCV (Fig. S4D and E), emphasizing a possible cross talk between the two

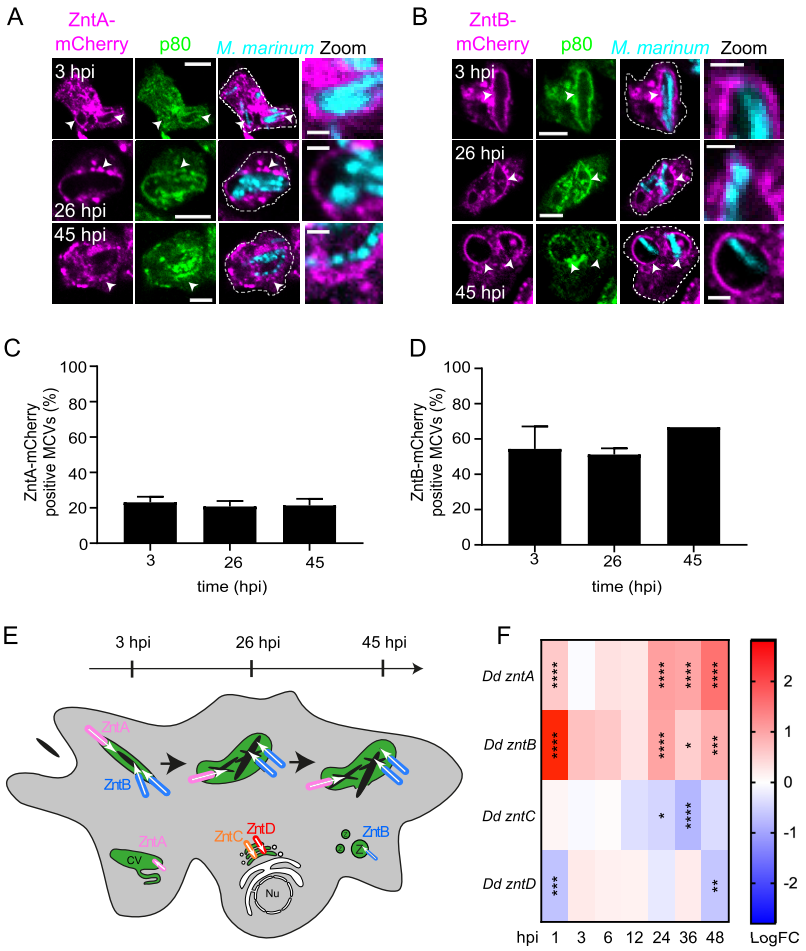

FIG 3 ZntA and ZntB transporters are recruited to the MCV and induced upon infection. (A and B) Immunofluorescence staining at different times postinfection of ZntA- or ZntB-mCherry-expressing cells (shown in magenta) infected with GFP-expressing *M. marinum* (shown in cyan). MCVs were visualized by staining for the endocytic marker p80 (21) (shown in green). Arrowheads mark Znt-positive MCVs. Scale bars, 5 μm (zoom, 2 μm). (C and D) Quantification of panels A and B, respectively. Two independent experiments were performed. 305 and 246 MCVs were analyzed manually for the presence of ZntA and ZntB at MCVs, respectively. (E) Scheme depicting the localization of the four *D. discoideum* Znts during infection with *M. marinum*. CV, contractile vacuole; Nu, nucleus. (F) Heat map representing the transcriptional data shown in Table S1C. Cells were either infected with GFP-expressing *M. marinum* wt or mock infected, and samples were collected at different hpi. The time points with statistically significant differential expression are marked with asterisks (*, $P < 0.05$; **, $P < 0.01$; ***, $P < 0.001$; ****, $P < 0.0001$). Colors indicate the strength of expression of *zntA* to *zntD* (in logFC) in infected cells compared to mock infected: from dark red (highest expression) to dark blue (lowest expression).

organelles. CV proteins were also found to be enriched in the MCV proteome (Fig. S4F and Table S2) (42). In addition, differential expression of genes encoding many CV proteins (38) suggests a role for this organelle during infection (Fig. S4F and Table S1B) (38).

In summary, the data suggest that ZntB is the main MCV Zn^{2+} transporter but that ZntA might also contribute to the import of Zn^{2+} into the MCV (summarizing scheme is in Fig. 3E).

The expression of *Dictyostelium* ZnTs is altered during infection with *M. marinum*. *M. marinum* infection in zebrafish modulates the expression of various Zn^{2+} transporters in granulomas (32). Further inspection of our dual RNA-Seq results of *D. discoideum* during infection with *M. marinum* (38) showed that the expression of *zntA* and *zntB* was upregulated at very early, mid-, and late stages of infection, with the highest levels found for *zntB* at 1 hpi (Fig. 3F and Table S1C) (38). In contrast, the expression of *zntC* and *zntD* was not or only weakly affected. We conclude that

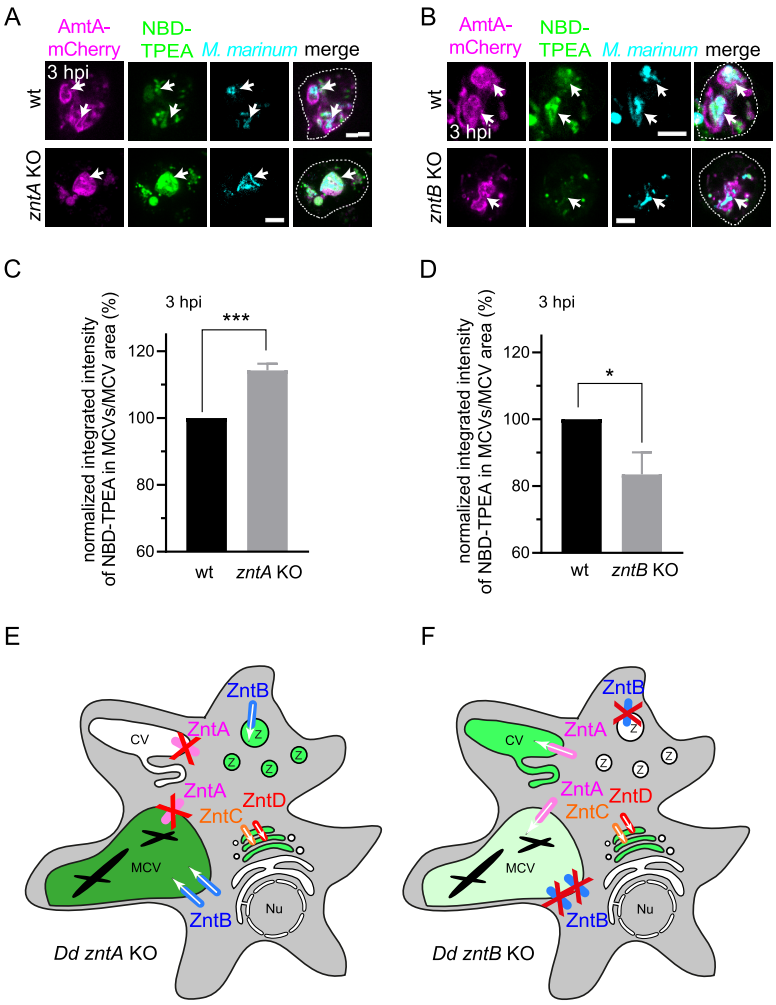

FIG 4 Zn^{2+} accumulates in MCVs of cells lacking ZntA but decreases in *zntB* KO amoebae. (A and B) Live imaging of NBD-TPEA-treated wt and *zntA* KO cells (A) or *zntB* KO cells (B) expressing AmtA-mCherry (magenta). *M. marinum* was stained with Vybrant DyeCycle Ruby (cyan) before imaging at 3 hpi (B) or 46 hpi (A). Arrows label MCVs. Scale bars, 5 μm. (C and D) Quantification of the normalized integrated intensity of NBD-TPEA inside MCVs per MCV area at 3 hpi in Ax2(Ka) wt and *zntA* KO cells (C) or Ax4 wt and *zntB* KO cells (D) infected with mCherry-expressing *M. marinum*. Images at 3 hpi were taken automatically using an ImageXpress spinning disc confocal microscope (Molecular Devices). To quantify NBD-TPEA inside MCVs, a MetaXpress (Molecular Devices) pipeline that detects NBD-TPEA inside MCVs was set up (see Materials and Methods). Four independent experiments were performed. A total of 7,353, 8,559, 5,713, and 4,679 MCVs were analyzed in infected Ax2(Ka) wt, Ax2(Ka) *zntA* KO, Ax4 wt, and Ax4 *zntB* KO cells, respectively. Statistical differences were assessed with an unpaired *t* test (*, $P < 0.05$; ***, $P < 0.001$). (E and F) Summarizing schemes illustrating the mislocalization of Zn^{2+} in infected *zntA* (E) or *zntB* (F) KO cells. While depletion of ZntA leads to an accumulation of Zn^{2+} into zincosomes and the MCV, loss of ZntB leads to a reduction of Zn^{2+} inside MCVs. Z, zincosomes; CV, contractile vacuole; MCV, *Mycobacterium*-containing vacuole; Nu, nucleus.

expression of ZntA and ZntB increases during *M. marinum* infection and also that their localization at the MCV contributes to the accumulation of Zn^{2+} inside the compartment. On the other hand, ZntC and ZntD, which are absent from the MCV, either are not relevant or might only play an indirect role by contributing to an accumulation of Zn^{2+} in other organelles that are linked to the MCV by membrane transport.

Knockout of ZntA and ZntB impact on the concentration of Zn^{2+} inside the MCV. We had previously shown that in the absence of ZntA, lumenal Zn^{2+} increases in acidic zincosomes and phagosomes, while in cells lacking ZntB, zincosomes contain low levels of Zn^{2+} (33). To determine the relevance of ZntA and ZntB in the restriction of *M. marinum* by Zn^{2+}, we infected cells lacking one or the other transporter and monitored the levels of Zn^{2+} inside early, intact MCVs (Fig. 4A to D). Similarly to bead-

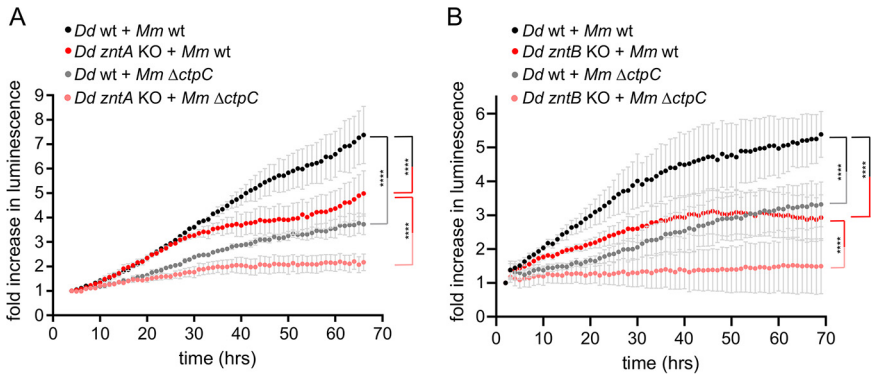

FIG 5 *M. marinum* intracellular growth is impaired in cells lacking ZntA or ZntB. Ax2(Ka) wt or *zntA* KO cells (A) and Ax4 wt or *zntB* KO cells (B) were infected with luciferase-expressing *M. marinum* wt or Δ*ctpC*, and the intracellular bacterial growth (in RLUs) was monitored every hour. Shown is the fold increase in bacterial luminescence over time. Error bars indicate the SEM from three independent experiments. Statistical differences of pairwise comparisons were calculated with a Fisher LSD *post hoc* test after two-way ANOVA (****, $P < 0.0001$).

containing phagosomes, MCVs accumulated more Zn^{2+} in *zntA* knockout (KO) cells while the levels of Zn^{2+} were lower in MCVs from *zntB* KO cells than from wt cells (Fig. 4A to D). This suggests that ZntB, the main lysosomal and postlysosomal Zn^{2+} transporter (33), might compensate for the absence of the main CV efflux detoxifier ZntA (33) by exporting Zn^{2+} into all endosomes and MCVs (summarizing schemes are in Fig. 4E and F).

Zn^{2+} restricts *M. marinum* during infection. Accumulation of higher Zn^{2+} levels in phagosomes of *D. discoideum zntA* KO cells results in a more efficient killing of the nonpathogenic bacterium *E. coli* (33). Plaque formation by *D. discoideum* on lawns of "food" bacteria spiked with pathogenic bacteria allows monitoring of either the virulence of the pathogen or the resistance/susceptibility of *D. discoideum* to these pathogens (43). Monitoring of plaque formation on lawns containing *M. marinum* confirmed that the *zntA* KO was less affected by the presence of *M. marinum* than wt *D. discoideum* (Fig. S5A and B). Interestingly, both *D. discoideum* wt and *zntA* KO grew better on lawns containing the attenuated *M. marinum* Δ*ctpC* mutant (Fig. S5A and B), confirming a Zn^{2+}-dependent defense process. In contrast, *D. discoideum zntB* KO cells did not benefit from a growth advantage on *M. marinum*-containing lawns (Fig. S5C and D), corroborating that the uptake, killing, and digestion of food bacteria are unaffected in these cells, although they have lower lumenal Zn^{2+} concentrations. Importantly, plaque formation on a variety of nonpathogenic bacteria was comparable for *zntA* KO, *zntB* KO, and wt cells (Fig. S5E and F). We conclude that the resistance of *D. discoideum* is proportional to both the level of Zn^{2+} within the MCV (which is higher in the *zntA* KO) and the capacity of *M. marinum* to detoxify its own intracellular Zn^{2+} (33).

Next, we monitored the impact of *znt* KOs on *M. marinum* intracellular growth. Strikingly, absence of ZntA led to a decrease in the intracellular load of *M. marinum* (Fig. 5A), suggesting that the bacteria encounter noxious levels of Zn^{2+} during infection (Fig. 4A and C). This was further corroborated by the fact that compared to *M. marinum* wt, the intracellular load of *M. marinum* Δ*ctpC*, which is more sensitive than wt to high Zn^{2+}-levels (Fig. 2C), was decreased in *zntA* KO cells (Fig. 5A). This epistatic interaction between *M. marinum* Δ*ctpC* and *D. discoideum zntA* KO (i.e., the higher growth restriction of Δ*ctpC* in the *zntA* KO compared to wt host) is strong evidence for the role of Zn^{2+} during infection.

Intriguingly, although the concentration of Zn^{2+} inside the MCVs was lower in cells lacking ZntB (Fig. 4B and D), the intracellular bacterial load also decreased with time in these mutant cells (Fig. 5B), comparably to what happens inside *zntA* KO cells (Fig. 5A).

But we also noticed that, while bacterial growth leveled off inside *zntA* KO cells only after 24 hpi (Fig. 5A), the growth of *M. marinum* in *zntB* KO cells was impaired from the beginning of the infection (Fig. 5B). One possible explanation is that phagosomal escape of *M. marinum* is altered in the *zntB* KO cells, exposing them either to a stronger restriction by cytosolic defenses in the case of an earlier escape (9, 44) or to a prolonged restriction by vacuolar Zn^{2+} is the case that MCV escape is inhibited.

To assess whether the MCV integrity is compromised in *D. discoideum* lacking *zntA* or *zntB*, we monitored selected readouts for MCV membrane damage and *M. marinum* cytosolic access (36, 44). In brief, membrane damage induced by *M. marinum* leads to bacterial and MCV ubiquitination and recruitment of the autophagy machinery (44). Consequently, the fraction of ubiquitin-positive mycobacteria is a proxy for damage. In addition, Plin, the *D. discoideum* homologue of mammalian perilipins, binds the hydrophobic mycobacterial cell wall when the mycobacteria are exposed to the cytosol (36). Interestingly, upon infection with *M. marinum* wt, the fractions of bacteria ubiquitinated or associated with Plin were comparable in all host cells (Fig. S6A to D), suggesting that membrane damage but also the detection of cytosolic bacteria is not affected in these mutants. In addition, no significant difference in ubiquitination was observed for the Δ*ctpC M. marinum* mutant, neither in wt nor in the *zntA* and *zntB* KO cells (Fig. S6A and B). However, a strong reduction of Plin-positive Δ*ctpC* bacteria was observed in *zntB* KO cells, suggesting that Δ*ctpC* might escape less efficiently to the cytosol in these cells (Fig. S6D). Nevertheless, the epistatic interaction observed between *M. marinum* Δ*ctpC* and *D. discoideum zntB* KO during the assessment of intracellular growth (Fig. 5B) suggests that Zn^{2+} plays a major role in the restriction of these bacteria also in the absence of *D. discoideum* ZntB.

DISCUSSION

Upon bacterial invasion, immune phagocytes manipulate their intracellular Zn^{2+} pools for nutritional immunity and/or metal intoxication purposes. Accordingly, infected neutrophils reduce *Streptococcus pyogenes* growth by releasing the Zn^{2+} scavenger calprotectin (45), while they enhance phagosomal Zn^{2+} levels for bacterial intoxication (46). Calprotectin also protects cells against other bacteria such as *Helicobacter pylori* (47), *Borrelia burgdorferi* (48), or *Staphylococcus aureus* (49). Using a different strategy, macrophages enhance bacterial clearance by delivering Zn^{2+} to *E. coli*-, *Salmonella enterica* serovar Typhimurium-, and Mtb-containing compartments (30, 50). However, pathogens have evolved mechanisms to counteract Zn^{2+}-mediated defenses. For instance, *Salmonella* evades Zn^{2+}-containing vesicles by means of its pathogenicity island 1 (SPI-1) (50), while Mtb exports Zn^{2+} through its P-type ATPase CtpC (30). In addition, upon calprotectin-mediated Zn^{2+} chelation, *Salmonella* induces the expression of its Zn^{2+} importer ZnuABC (51). In this study, we focused on the Zn^{2+}-mediated battle between *M. marinum* and its experimental host *D. discoideum*.

D. discoideum is a model to study the role of transition metals in the fight against intracellular pathogens (35, 52–54). For example, while Fe^{2+} participates in the defense against *Mycobacterium avium* or *Legionella pneumophila* (35, 52–54), Cu^{2+} or Zn^{2+} does not affect the infection by *Legionella* (35). On the other hand, to access poorly available transition metals such as iron, *M. marinum* stimulates the synthesis and release of small chelating molecules known as siderophores (55).

In contrast to the 24 transporters encoded in humans, *D. discoideum* possesses only 11 Zn^{2+} transporters: seven ZIP-like proteins (ZplA to -G) and four ZnTs (ZntA to -D) (4). ZntA is the main transporter in the CV and a key regulator of Zn^{2+} homeostasis in *D. discoideum*. The transporter is not found in the endocytic and phagocytic pathways in noninfected cells. When ZntA is knocked out, cells compensate for its absence by increasing pumping of Zn^{2+} inside the compartments of the endocytic pathway through the other transporters ZntB to ZntD (33). ZntB is the main Zn^{2+} importer in lysosomes and recycling endosomes (33). Interestingly, throughout the intracellular infection cycle of *M. marinum*, both ZntA and ZntB were located at MCVs (Fig. 3A to E),

although at different levels. While ZntA localized at detectable levels only to a minor fraction of MCVs (around 20% [Fig. 3C]), ZntB was present at the majority of them (50 to 60% [Fig. 3D]). This, together with the fact that the expression of ZntB notably increased during *M. marinum* infection (Fig. 3F) and that MCVs accumulate less Zn^{2+} in cells lacking ZntB (Fig. 4B, D, and F), led us to hypothesize that ZntB is the main Zn^{2+} efflux transporter during infection by *M. marinum*, directly pumping Zn^{2+} into the MCVs. Since accumulation of Zn^{2+} within MCVs was not completely abolished upon ZntB depletion, we propose that Zn^{2+} can also be transferred into MCVs by direct transport via ZntA, especially considering that the levels of the *zntA* mRNA increase at all stages of infection (Fig. 2A). In addition, fusion of MCVs with zincosomes, as shown to occur to the *M. smegmatis*-containing compartment (33), might also contribute to elevated lumenal Zn^{2+} levels. As ZntC and ZntD are localized to other compartments of the endocytic and secretory pathways, they could indirectly contribute to lumenal Zn^{2+} levels (33). But a direct role of these transporters can likely be disregarded, because ZntC and ZntD were not detected at the MCV at any time postinfection (Fig. 3E and see also Fig. S4A and B in the supplemental material), and the levels of their mRNA were not altered, or only slightly reduced, during infection with *M. marinum* (Fig. 3F and Table S1C). Previous studies have shown that the expression of ZNT1, the homologue of ZntB, increases in human macrophages after 18 and 72 h of infection with Mtb (26, 30, 32). This suggests that *D. discoideum* reacts to the invasion by pathogenic mycobacteria in a manner similar to mammalian macrophages.

The complex Zn^{2+} homeostasis is regulated by the balance of ZnT efflux transporters and ZIP influx transporters. In other words, higher ZIP-mediated pumping of Zn^{2+} to the cytosol is compensated for by detoxification, via ZnT-mediated import of Zn^{2+} inside various compartments, including the MCV. On the other hand, decreased ZIP-mediated transport from endosomes to the cytosol might also increase lumenal Zn^{2+}. In keeping with these scenarios, the expression of many of the *D. discoideum* Zpl influx pumps is affected in complex manners during infection with *M. marinum* (Fig. S7 and Table S1D).

We show here that, *in vitro*, *M. marinum* senses and reacts to elevated levels of Zn^{2+} by specifically inducing the expression of the Zn^{2+} efflux pump CtpC (Fig. 2B). Accordingly, growth of *M. marinum* Δ*ctpC* was inhibited at elevated concentrations of Zn^{2+} (Fig. 2C). Importantly, this growth inhibition was fully rescued by expressing the Mtb CtpC (Rv3270), confirming that CtpC (MMAR_1271) is its functional orthologue in Zn^{2+} efflux in *M. marinum* (Fig. 2C and D). Increasing concentrations of Mn^{2+} did not affect growth of *M. marinum* wt, nor that of the Δ*ctpC* mutant (Fig. S3F), excluding that *M. marinum* CtpC is a manganese exporter as was previously claimed for Mtb CtpC (56).

As shown for Mtb, *M. marinum ctpC* is also induced during infection of *D. discoideum* (Fig. 2A), and deletion of *ctpC* strongly attenuates intracellular growth of *M. marinum* (Fig. 2D). This indicates that, inside amoebae, *M. marinum* experiences toxic concentrations of Zn^{2+}, which it resists by exporting Zn^{2+} through CtpC. Our results further demonstrate that MCV damage leads to the efflux of Zn^{2+} to the cytosol at early infection stages (Fig. 1), suggesting that the transient exposure to high Zn^{2+} levels is sufficient to stimulate *ctpC* expression. Therefore, it appears that *M. marinum* makes use of an integrated strategy to counteract the intoxication by Zn^{2+} in the MCV, first by increasing CtpC-mediated efflux into the MCV lumen and second by inducing ESAT-6-dependent MCV damage, resulting in leakage of ions (H^+, Zn^{2+}, and others) to the cytosol. This model is in line with a previous study (57) showing that accumulation of Zn^{2+} in Mtb-infected fibroblasts leads both to the upregulation of CtpC and to an increased secretion of ESAT-6 that results in phagosomal damage and ion efflux.

Strikingly, the intracellular growth of *M. marinum* wt was similarly impaired in amoebae lacking ZntA or ZntB (Fig. 5), although the levels of Zn^{2+} inside MCVs were higher in the *D. discoideum zntA* KO but lower in the *zntB* KO, compared to wt (Fig. 4). We propose the following model to account for this apparently counterintuitive result.

First, the fact that an *M. marinum* mutant in a Zn-related gene (*ctpC*) is even more attenuated for intracellular growth in a *D. discoideum* mutant itself affected in a Zn-related gene (*zntA* or *zntB*) is a demonstration that the two mutants interact genetically in a way that is best explainable by a dual perturbation in Zn^{2+} homeostasis. Second, the increased attenuation of the Δ*ctpC* mutant in the *zntA* KO host is most likely due to the elevated MCV Zn^{2+} concentration, while the increased attenuation in the *zntB* KO is likely due to inefficient MCV escape and prolonged exposure to the residual lumenal Zn^{2+} concentration.

In summary, we conclude that *D. discoideum* restricts an infection with *M. marinum* by using one or more Zn^{2+}-dependent host defense mechanisms, which are counteracted by the pathogen via the specific induction of its Zn^{2+} exporter CtpC. To our knowledge, this is the first study reporting the role of CtpC in the resistance of *M. marinum* to Zn^{2+}-mediated host defense.

MATERIALS AND METHODS

***D. discoideum* strains, culture, and plasmids.** The *D. discoideum* material used in this study is listed in Table S3A in the supplemental material. The wt strains Ax2(Ka) and Ax4 were grown at 22°C in HL5-C medium (Formedium) supplemented with 100 U/ml penicillin and 100 μg/ml streptomycin. Overexpressers and KO cell lines were grown in medium with hygromycin (25 μg/ml), G418 (5 μg/ml), and/or blasticidin (5 μg/ml).

***Mycobacterium* strains, culture, and plasmids.** The *M. marinum* strains and plasmids used in the present study are listed in Table S3B. *M. marinum* Δ*ctpC* was generated by specialized phage transduction as previously described (Table S3B) (19) with modifications. The flanking regions of *ctpC* were amplified using the primer pairs oHK143/oHK144 and oHK145/oHK146 (Table S3B). The PCR products were digested with AlwNI and Van91I, respectively, and ligated with Van91I-digested p0004S vector fragments. The resulting plasmid pHK42 and the DNA of the temperature-sensitive phage phAE159 were ligated after previous linearization with PacI, gaining pHK50. High-titer phages of pHK50 were prepared in *M. smegmatis* to perform specialized transduction in *M. marinum*, finally yielding the Δ*ctpC*::Hyg^r mutant. The phAE7.1 phage was used to remove the Hyg^r cassette (19). Primers used for mutant verification are listed in Table S3B (oHK159, oHK160, oHK33, and oHK36). A complementation vector was generated by the FX-cloning strategy (58) using the backbone pFLAG plasmid (59) to constitutively expresses the Mtb orthologue of *ctpC* (Rv3270) from the medium-strength tetracycline promoter. The vector is then stably integrated into the genomic *attB* site. Mtb *ctpC* was amplified from genomic DNA using the primer pair oHK375/oHK376 to yield pHK124. The correct insertion was verified by sequencing using the primers oHK328, oHK340, and oHK377. Mycobacteria were cultured at 150 rpm at 32°C in Middlebrook 7H9 (Difco) supplemented with 10% oleic acid-albumin-dextrose-catalase (OADC), 0.2% glycerol, and 0.05% Tween 80. Bacterial clumping was minimized by adding 5-mm glass beads during cultivation. Mutants and plasmid carriers were grown in medium supplemented with hygromycin (100 μg/ml), kanamycin (25 μg/ml), and/or ampicillin (100 μg/ml).

***M. marinum* growth on agar and in broth.** *M. marinum* wt and Δ*ctpC* were grown in liquid 7H9-OADC-glycerol-Tween at 32°C in shaking until reaching an optical density at 600 nm (OD_{600}) of approximately 0.5. For growth assays on agar, serial 10-fold dilutions were performed and 5 μl of each dilution was plated on 7H11-OADC-glycerol-Tween containing different concentrations (0, 0.125, 0.250, 0.500, 1.000, and 2.50 mM) of $ZnSO_4$, $MnCl_2$, and $CuSO_4$. Pictures were taken after 7 days of incubation at 32°C. For growth in broth, overnight cultures of green fluorescent protein (GFP)-expressing *M. marinum* wt and Δ*ctpC* as well as of E2-Crimson (pTEC19, Addgene)-expressing wt and Δ*ctpC*::*ctpC* were diluted to 5×10^5 bacteria/ml, centrifuged, and resuspended in 7H9 medium containing increasing $ZnSO_4$ concentrations as indicated. Bacteria were distributed in 96-well plates at 10^5/well (Perkin Elmer). Growth at 32°C under shaking conditions was assessed by measuring fluorescence at 509 nm for the GFP signal and 646 nm for the E2-Crimson signal in a plate reader (Synergy MX; BioTek). The growth of the Δ*ctpC* (GFP) and Δ*ctpC*::*ctpC* (E2-Crimson) strains was normalized to the *M. marinum* wt strains expressing GFP and E2-Crimson, respectively.

Infection of *D. discoideum*. Infections were performed as previously described (21, 60). After spinoculation and washing off the extracellular bacteria, the infected cells were resuspended at a density of 1×10^6 cells/ml in filtered HL5-C. Five micrograms per milliliter of streptomycin and 5 U/ml of penicillin were added to prevent extracellular bacterial growth. The infected cells were then incubated at 25°C at 130 rpm, and samples were taken for analysis at the indicated time points.

Live cell imaging. To monitor the subcellular localization of Zn^{2+} during infection, infected cells were plated on μ-dishes (ibidi), medium was exchanged to Soerensen buffer, and intracellular Zn^{2+} was stained with 5 μM NBD-TPEA (Sigma catalog no. N1040 [61]) for 30 min in the dark (33). To stain unlabeled bacteria, Vybrant DyeCycle Ruby stain (ThermoFisher) was used as previously described (3). Escape of *M. marinum* from MCVs was assessed in cells expressing mCherry-Plin. Images of live cells were taken with an inverted 3i Marianas spinning disc confocal microscope using the 63× glycerol or 100× oil objectives. Fluorescent proteins or probes were excited using the 488-nm (GFP and NBD-TPEA), 561-nm (mCherry), and 640-nm (Vybrant Ruby) laser lines, respectively. To quantify the integrated intensity of NBD-TPEA inside MCVs, cells were infected with mCherry-expressing *M. marinum*. At the indicated

time points, samples were stained with NBD-TPEA and images were taken using the ImageXpress spinning disc confocal microscope (Molecular Devices). Here, mCherry-expressing bacteria were excited using the Texas Red laser line and NBD-TPEA-expressing bacteria were excited using the GFP laser line. The integrated intensity per MCV area was assessed using an analysis pipeline created in MetaXpress Custom Module Editor (Molecular Devices). Briefly, MCVs were defined as a sphere around mCherry-labeled bacteria that were detected using the Texas Red channel. NBD-TPEA inside MCVs was detected using the settings for the GFP channel. The normalized integrated intensity of NBD-TPEA was divided by the area of each MCV, leading to the integrated intensity per MCV area.

Antibodies and immunofluorescence. Antibodies against p80 (62) were from the Geneva Antibody Facility (University of Geneva, Switzerland); anti-Ub (FK2) monoclonal antibodies were from Enzo Life Sciences. The mCherry fluorescent signal was enhanced with rat monoclonal (MAb) anti-red fluorescent protein (anti-RFP) antibodies (Chromotek). As secondary antibodies, goat anti-rabbit, anti-mouse, and anti-rat IgG coupled to Alexa 488 or Alexa 546 (Thermo Fisher Scientific) or CF640R (Biotium) were used. Cells were fixed with cold methanol (MeOH) as described previously (40). Images were recorded with Zeiss LSM700 and LSM800 confocal microscopes and a 63×/1.4-numerical-aperture (NA) or a 100×/1.4-NA oil-immersion objective. Fluorescent proteins or secondary antibodies were excited using the 405-nm (DAPI), 488-nm (GFP and Alexa 488), 555-nm (Alexa 546), and 639-nm (CF640R) laser lines.

RNA-sequencing data. RNA-Seq data were gathered from the work of Hanna et al. (38). Briefly, infection was carried out using *M. marinum* expressing GFP as described above. In brief, at each time point, a homogeneous population of infected cells was obtained by GFP fluorescence-activated cell sorting (FACS). The total RNA was extracted, and the rRNA from host and bacteria was depleted, before generation of the cDNA libraries using a Bio-Rad iScript kit and sequencing. The resulting reads were mapped in parallel against the *D. discoideum* and *M. marinum* genome. Differential expression analysis of the infection time course was performed using the R package limma, by comparing on one hand infected *D. discoideum* cells to mock (i.e., buffer)-infected cells, and on the other hand intracellular *M. marinum* to *M. marinum* grown in broth.

qRT-PCR sample collection and analysis. To assess the effect of Zn^{2+} on the expression of *ctpC*, *ctpC*-like, *ctpV*, and *ctpV*-like, *M. marinum* strains were exposed to various concentrations of $ZnSO_4$ (0.00, 0.05, 0.10, and 0.50 mM) for 2 h. Bacteria were harvested, RNA was extracted, and cDNA was synthesized using a Bio-Rad iScript kit. For each gene tested, the mean calculated threshold cycles (C_T) were averaged and normalized to the C_T of a gene with constant expression (*sigA*). The normalized C_T was used for calculating the fold change using the $\Delta\Delta C_T$ method. Briefly, relative levels of target mRNA, normalized with respect to an endogenous control (*sigA*), were expressed as $2-\Delta\Delta C_T$ (fold), where $\Delta C_T = C_T$ of the target gene $- C_T$ of the control gene (*sigA*), and $\Delta\Delta C_T = \Delta C_T$ of the studied set of conditions $- \Delta C_T$ of the calibrator conditions, as previously described (63).

Measurement of intracellular bacterial growth. Intracellular growth of *M. marinum* expressing fluorescent reporters or bacterial luciferase was measured as previously described (64). Briefly, three different dilutions of infected cells (between 0.5×10^5 and 2.0×10^5 cells) were plated on nontreated, white F96 MicroWell plates (Nunc) or black 96-well plates (Perkin Elmer) covered with a gas-permeable moisture barrier seal (BioConcept). The course of infection was monitored by measuring either luminescence or fluorescence (at 509 and 646 nm) as a proxy of bacterial growth using a Synergy Mx microplate reader (BioTek) at a constant temperature of 25°C for around 70 h with 1-h intervals. The growth of the Δ*ctpC* (GFP) and Δ*ctpC*::*ctpC* (E2-Crimson) strains was normalized to *M. marinum* wt strains expressing GFP and E2-Crimson, respectively.

Phagocytic plaque assay. Phagocytic plaque assays in the presence of nonpathogenic bacteria as food source were performed as described previously (43). Briefly, 50 μl of an overnight culture of various nonpathogenic bacteria was added to the wells of a 24-well plate containing 2 ml SM-agar. Then, 10, 100, 1,000, or 10,000 *D. discoideum* cells were added to the bacterial lawn and plates were incubated at 22°C for 4 to 7 days until plaques were visible. Quantification was performed by scoring the appearance of plaques in at least three independent experiments. The logarithmic plaquing score was defined as follows: plaque formation in wells with 10 amoebae yielded a score of 1,000; in the cases where cells did not grow at lower dilutions, they obtained the corresponding lower scores of 100, 10, and 1. The ability of *D. discoideum* Ax2(Ka), *zntA* KO, Ax4, and *zntB* KO to form plaques on *M. marinum* wt and Δ*ctpC* was assessed as described previously (43, 65). Briefly, 5×10^8 mycobacteria were harvested and resuspended in 1.2 ml of 7H9-OADC-glycerol-Tween containing a $1{:}10^5$ dilution of an overnight culture of *Klebsiella pneumoniae*. Fifty microliters of the suspension was added to the wells of a 24-well plate containing 2 ml of 7H11-OADC-glycerol-Tween. Various dilutions of *D. discoideum* (i.e., 10, 100, 1,000, and 10,000 cells; for strains in the Ax4 background, 3-fold more cells were used to achieve similar temporal evolution of the plaques) were added to the bacterial lawn, and plates were incubated at 25°C for 7 days until plaques were visible. The scoring was performed as described above.

Phylogenetic tree. Putative P-type ATPases of *M. marinum* were identified by performing a protein BLAST search using NCBI PSI-BLAST and the sequence of Mtb CtpC. The results were then cross-compared to the annotations of *M. marinum* P-type ATPases available on Mycobrowser (66). The protein sequences of Mtb and *M. marinum* P-type ATPases were aligned with the online version of MAFFT (https://mafft.cbrc.jp/alignment/server/) using the G-INS-1 strategy and "leave gappy regions" to generate a phylogenetic tree in phylo.ilo using NJ conserved sites and the JTT substitution model (67).

Data availability. Information on the differential expression of *M. marinum* P-type ATPases (Table S1A) as well as *D. discoideum* CV genes (Table S1B), *zntA* to *-D* transporters (Table S1C), and *zplA* to *-G* transporters (Table S1D) was extracted from the preprint resource at https://doi.org/10.1101/

590810 (38). Information on the enrichment of CV proteins at the MCV (Table S2) was extracted from the preprint resource at https://doi.org/10.1101/592717 (42).

SUPPLEMENTAL MATERIAL

Supplemental material is available online only.

FIG S1, PDF file, 0.03 MB.
FIG S2, PDF file, 0.2 MB.
FIG S3, PDF file, 0.9 MB.
FIG S4, PDF file, 0.7 MB.
FIG S5, PDF file, 0.2 MB.
FIG S6, PDF file, 0.06 MB.
FIG S7, PDF file, 0.04 MB.
TABLE S1, DOCX file, 0.03 MB.
TABLE S2, DOCX file, 0.01 MB.
TABLE S3, DOCX file, 0.03 MB.

ACKNOWLEDGMENTS

We gratefully acknowledge Dimitri Moreau at the ACCESS imaging platform and the Bioimaging Center of the University of Geneva for their expert and friendly support.

This work was supported by Swiss National Science Foundation (SNF) grants 310030_169386 and 310030_188813 (awarded to T.S.) and an RTD grant from SystemsX.ch (HostPathX, awarded to H.H. and T.S.). TS is a member of iGE3 (http://www.ige3.unige.ch). The funders had no role in study design, data collection and analysis, decision to publish, or preparation of the manuscript.

REFERENCES

1. Aubry A, Mougari F, Reibel F, Cambau E. 2017. *Mycobacterium marinum*. Microbiol Spectr 5(2). https://doi.org/10.1128/microbiolspec.TNMI7-0038-2016.
2. Tobin DM, Ramakrishnan L. 2008. Comparative pathogenesis of Mycobacterium marinum and Mycobacterium tuberculosis. Cell Microbiol 10:1027–1039. https://doi.org/10.1111/j.1462-5822.2008.01133.x.
3. Cardenal-Muñoz E, Barisch C, Lefrançois LH, López-Jiménez AT, Soldati T. 2018. When Dicty met Myco, a (not so) romantic story about one amoeba and its intracellular pathogen. Front Cell Infect Microbiol 7:529. https://doi.org/10.3389/fcimb.2017.00529.
4. Dunn JD, Bosmani C, Barisch C, Raykov L, Lefrançois LH, Cardenal-Muñoz E, López-Jiménez AT, Soldati T. 2017. Eat prey, live: Dictyostelium discoideum as a model for cell-autonomous defenses. Front Immunol 8:1906. https://doi.org/10.3389/fimmu.2017.01906.
5. Russell DG. 2001. *Mycobacterium tuberculosis*: here today, and here tomorrow. Nat Rev Mol Cell Biol 2:569–577. https://doi.org/10.1038/35085034.
6. Stamm LM, Morisaki JH, Gao L-Y, Jeng RL, McDonald KL, Roth R, Takeshita S, Heuser J, Welch MD, Brown EJ. 2003. *Mycobacterium marinum* escapes from phagosomes and is propelled by actin-based motility. J Exp Med 198:1361–1368. https://doi.org/10.1084/jem.20031072.
7. Smith J, Manoranjan J, Pan M, Bohsali A, Xu J, Liu J, McDonald KL, Szyk A, LaRonde-LeBlanc N, Gao L-Y. 2008. Evidence for pore formation in host cell membranes by ESX-1-secreted ESAT-6 and its role in *Mycobacterium marinum* escape from the vacuole. Infect Immun 76:5478–5487. https://doi.org/10.1128/IAI.00614-08.
8. Hagedorn M, Rohde KH, Russell DG, Soldati T. 2009. Infection by tubercular mycobacteria is spread by nonlytic ejection from their amoeba hosts. Science 323:1729–1733. https://doi.org/10.1126/science.1169381.
9. López-Jiménez AT, Cardenal-Muñoz E, Leuba F, Gerstenmaier L, Barisch C, Hagedorn M, King JS, Soldati T. 2018. The ESCRT and autophagy machineries cooperate to repair ESX-1-dependent damage at the Mycobacterium-containing vacuole but have opposite impact on containing the infection. PLoS Pathog 14:e1007501. https://doi.org/10.1371/journal.ppat.1007501.
10. van der Wel N, Hava D, Houben D, Fluitsma D, van Zon M, Pierson J, Brenner M, Peters PJ. 2007. *M. tuberculosis* and *M. leprae* translocate from the phagolysosome to the cytosol in myeloid cells. Cell 129:1287–1298. https://doi.org/10.1016/j.cell.2007.05.059.
11. Simeone R, Bobard A, Lippmann J, Bitter W, Majlessi L, Brosch R, Enninga J. 2012. Phagosomal rupture by *Mycobacterium tuberculosis* results in toxicity and host cell death. PLoS Pathog 8:e1002507. https://doi.org/10.1371/journal.ppat.1002507.
12. Houben D, Demangel C, van Ingen J, Perez J, Baldeón L, Abdallah AM, Caleechurn L, Bottai D, van Zon M, de Punder K, van der Laan T, Kant A, Bossers-de Vries R, Willemsen P, Bitter W, van Soolingen D, Brosch R, van der Wel N, Peters PJ. 2012. ESX-1-mediated translocation to the cytosol controls virulence of mycobacteria. Cell Microbiol 14:1287–1298. https://doi.org/10.1111/j.1462-5822.2012.01799.x.
13. Mittal E, Skowyra ML, Uwase G, Tinaztepe E, Mehra A, Köster S, Hanson PI, Philips JA. 2018. *Mycobacterium tuberculosis* type VII secretion system effectors differentially impact the ESCRT endomembrane damage response. mBio 9:e01765-18. https://doi.org/10.1128/mBio.01765-18.
14. Grayfer L, Hodgkinson JW, Belosevic M. 2011. Analysis of the antimicrobial responses of primary phagocytes of the goldfish (*Carassius auratus* L.) against *Mycobacterium marinum*. Dev Comp Immunol 35:1146–1158. https://doi.org/10.1016/j.dci.2011.04.007.
15. Yang C-T, Cambier CJ, Davis JM, Hall CJ, Crosier PS, Ramakrishnan L. 2012. Neutrophils exert protection in the early tuberculous granuloma by oxidative killing of mycobacteria phagocytosed from infected macrophages. Cell Host Microbe 12:301–312. https://doi.org/10.1016/j.chom.2012.07.009.
16. Lerena MC, Colombo MI. 2011. *Mycobacterium marinum* induces a marked LC3 recruitment to its containing phagosome that depends on a functional ESX-1 secretion system. Cell Microbiol 13:814–835. https://doi.org/10.1111/j.1462-5822.2011.01581.x.
17. Thi EP, Hong CJH, Sanghera G, Reiner NE. 2013. Identification of the *Mycobacterium tuberculosis* protein PE-PGRS62 as a novel effector that functions to block phagosome maturation and inhibit iNOS expression. Cell Microbiol 15:795–808. https://doi.org/10.1111/cmi.12073.
18. Robinson N, Wolke M, Ernestus K, Plum G. 2007. A mycobacterial gene involved in synthesis of an outer cell envelope lipid is a key factor in prevention of phagosome maturation. Infect Immun 75:581–591. https://doi.org/10.1128/IAI.00997-06.
19. Koliwer-Brandl H, Knobloch P, Barisch C, Welin A, Hanna N, Soldati T, Hilbi H. 2019. Distinct *Mycobacterium marinum* phosphatases determine pathogen vacuole phosphoinositide pattern, phagosome maturation and escape to the cytosol. Cell Microbiol 21:e13008. https://doi.org/10.1111/cmi.13008.

20. Vieira OV, Harrison RE, Scott CC, Stenmark H, Alexander D, Liu J, Gruenberg J, Schreiber AD, Grinstein S. 2004. Acquisition of Hrs, an essential component of phagosomal maturation, is impaired by mycobacteria. Mol Cell Biol 24:4593–4604. https://doi.org/10.1128/mcb.24.10.4593-4604.2004.
21. Hagedorn M, Soldati T. 2007. Flotillin and RacH modulate the intracellular immunity of *Dictyostelium* to *Mycobacterium marinum* infection. Cell Microbiol 9:2716–2733. https://doi.org/10.1111/j.1462-5822.2007.00993.x.
22. Tan T, Lee WL, Alexander DC, Grinstein S, Liu J. 2006. The ESAT-6/CFP-10 secretion system of *Mycobacterium marinum* modulates phagosome maturation. Cell Microbiol 8:1417–1429. https://doi.org/10.1111/j.1462-5822.2006.00721.x.
23. Wagner D, Maser J, Lai B, Cai Z, Barry CE, Höner Zu Bentrup K, Russell DG, Bermudez LE. 2005. Elemental analysis of *Mycobacterium avium*-, *Mycobacterium tuberculosis*-, and *Mycobacterium smegmatis*-containing phagosomes indicates pathogen-induced microenvironments within the host cell's endosomal system. J Immunol 174:1491–1500. https://doi.org/10.4049/jimmunol.174.3.1491.
24. Wolschendorf F, Ackart D, Shrestha TB, Hascall-Dove L, Nolan S, Lamichhane G, Wang Y, Bossmann SH, Basaraba RJ, Niederweis M. 2011. Copper resistance is essential for virulence of *Mycobacterium tuberculosis*. Proc Natl Acad Sci U S A 108:1621–1626. https://doi.org/10.1073/pnas.1009261108.
25. Neyrolles O, Wolschendorf F, Mitra A, Niederweis M. 2015. Mycobacteria, metals, and the macrophage. Immunol Rev 264:249–263. https://doi.org/10.1111/imr.12265.
26. Pyle CJ, Azad AK, Papp AC, Sadee W, Knoell DL, Schlesinger LS. 2017. Elemental ingredients in the macrophage cocktail: role of ZIP8 in host response to *Mycobacterium tuberculosis*. Int J Mol Sci 18:2375. https://doi.org/10.3390/ijms18112375.
27. Sritharan M. 2016. Iron homeostasis in *Mycobacterium tuberculosis*: mechanistic insights into siderophore-mediated iron uptake. J Bacteriol 198:2399–2409. https://doi.org/10.1128/JB.00359-16.
28. Ward SK, Abomoelak B, Hoye EA, Steinberg H, Talaat AM. 2010. CtpV: a putative copper exporter required for full virulence of Mycobacterium tuberculosis. Mol Microbiol 77:1096–1110. https://doi.org/10.1111/j.1365-2958.2010.07273.x.
29. Gold B, Deng H, Bryk R, Vargas D, Eliezer D, Roberts J, Jiang X, Nathan C. 2008. Identification of a copper-binding metallothionein in pathogenic mycobacteria. Nat Chem Biol 4:609–616. https://doi.org/10.1038/nchembio.109.
30. Botella H, Peyron P, Levillain F, Poincloux R, Poquet Y, Brandli I, Wang C, Tailleux L, Tilleul S, Charrière GM, Waddell SJ, Foti M, Lugo-Villarino G, Gao Q, Maridonneau-Parini I, Butcher PD, Castagnoli PR, Gicquel B, de Chastellier C, Neyrolles O. 2011. Mycobacterial p(1)-type ATPases mediate resistance to zinc poisoning in human macrophages. Cell Host Microbe 10:248–259. https://doi.org/10.1016/j.chom.2011.08.006.
31. Botella H, Stadthagen G, Lugo-Villarino G, de Chastellier C, Neyrolles O. 2012. Metallobiology of host-pathogen interactions: an intoxicating new insight. Trends Microbiol 20:106–112. https://doi.org/10.1016/j.tim.2012.01.005.
32. Cronan MR, Beerman RW, Rosenberg AF, Saelens JW, Johnson MG, Oehlers SH, Sisk DM, Jurcic Smith KL, Medvitz NA, Miller SE, Trinh LA, Fraser SE, Madden JF, Turner J, Stout JE, Lee S, Tobin DM. 2016. Macrophage epithelial reprogramming underlies mycobacterial granuloma formation and promotes infection. Immunity 45:861–876. https://doi.org/10.1016/j.immuni.2016.09.014.
33. Barisch C, Kalinina V, Lefrançois LH, Appiah J, López-Jiménez AT, Soldati T. 2018. Localization of all four ZnT zinc transporters in *Dictyostelium* and impact of ZntA and ZntB knockout on bacteria killing. J Cell Sci 131:jcs222000. https://doi.org/10.1242/jcs.222000.
34. Peracino B, Buracco S, Bozzaro S. 2013. The Nramp (Slc11) proteins regulate development, resistance to pathogenic bacteria and iron homeostasis in *Dictyostelium discoideum*. J Cell Sci 126:301–311. https://doi.org/10.1242/jcs.116210.
35. Buracco S, Peracino B, Andreini C, Bracco E, Bozzaro S. 2017. Differential effects of iron, zinc, and copper on *Dictyostelium discoideum* cell growth and resistance to *Legionella pneumophila*. Front Cell Infect Microbiol 7:536. https://doi.org/10.3389/fcimb.2017.00536.
36. Barisch C, Paschke P, Hagedorn M, Maniak M, Soldati T. 2015. Lipid droplet dynamics at early stages of *Mycobacterium marinum* infection in *Dictyostelium*. Cell Microbiol 17:1332–1349. https://doi.org/10.1111/cmi.12437.
37. Tailleux L, Waddell SJ, Pelizzola M, Mortellaro A, Withers M, Tanne A, Castagnoli PR, Gicquel B, Stoker NG, Butcher PD, Foti M, Neyrolles O. 2008. Probing host pathogen cross-talk by transcriptional profiling of both *Mycobacterium tuberculosis* and infected human dendritic cells and macrophages. PLoS One 3:e1403. https://doi.org/10.1371/journal.pone.0001403.
38. Hanna N, Burdet F, Melotti A, Bosmani C, Kicka S, Hilbi H, Cosson P, Pagni M, Soldati T. 2019. Time-resolved RNA-seq profiling of the infection of *Dictyostelium discoideum* by *Mycobacterium marinum* reveals an integrated host response to damage and stress. bioRxiv https://doi.org/10.1101/590810.
39. Neuhaus EM, Horstmann H, Almers W, Maniak M, Soldati T. 1998. Ethane-freezing/methanol-fixation of cell monolayers: a procedure for improved preservation of structure and antigenicity for light and electron microscopies. J Struct Biol 121:326–342. https://doi.org/10.1006/jsbi.1998.3971.
40. Hagedorn M, Neuhaus EM, Soldati T. 2006. Optimized fixation and immunofluorescence staining methods for *Dictyostelium* cells. Methods Mol Biol 346:327–338. https://doi.org/10.1385/1-59745-144-4:327.
41. Du F, Edwards K, Shen Z, Sun B, De Lozanne A, Briggs S, Firtel RA. 2008. Regulation of contractile vacuole formation and activity in *Dictyostelium*. EMBO J 27:2064–2076. https://doi.org/10.1038/emboj.2008.131.
42. Guého A, Bosmani C, Soldati T. 2019. Proteomic characterization of the Mycobacterium marinum-containing vacuole in *Dictyostelium discoideum*. bioRxiv https://doi.org/10.1101/592717.
43. Froquet R, Lelong E, Marchetti A, Cosson P. 2009. *Dictyostelium discoideum*: a model host to measure bacterial virulence. Nat Protoc 4:25–30. https://doi.org/10.1038/nprot.2008.212.
44. Cardenal-Munoz E, Arafah S, López-Jiménez AT, Kicka S, Falaise A, Bach F, Schaad O, King JS, Hagedorn M, Soldati T. 2017. *Mycobacterium marinum* antagonistically induces an autophagic response while repressing the autophagic flux in a TORC1- and ESX-1-dependent manner. PLoS Pathog 13:e1006344. https://doi.org/10.1371/journal.ppat.1006344.
45. Makthal N, Nguyen K, Do H, Gavagan M, Chandrangsu P, Helmann JD, Olsen RJ, Kumaraswami M. 2017. A critical role of zinc importer AdcABC in group A Streptococcus-host interactions during infection and its implications for vaccine development. EBioMedicine 21:131–141. https://doi.org/10.1016/j.ebiom.2017.05.030.
46. Ong C-LY, Gillen CM, Barnett TC, Walker MJ, McEwan AG. 2014. An antimicrobial role for zinc in innate immune defense against group A streptococcus. J Infect Dis 209:1500–1508. https://doi.org/10.1093/infdis/jiu053.
47. Gaddy JA, Radin JN, Loh JT, Piazuelo MB, Kehl-Fie TE, Delgado AG, Ilca FT, Peek RM, Cover TL, Chazin WJ, Skaar EP, Scott Algood HM. 2014. The host protein calprotectin modulates the *Helicobacter pylori cag* type IV secretion system via zinc sequestration. PLoS Pathog 10:e1004450. https://doi.org/10.1371/journal.ppat.1004450.
48. Lusitani D, Malawista SE, Montgomery RR. 2003. Calprotectin, an abundant cytosolic protein from human polymorphonuclear leukocytes, inhibits the growth of *Borrelia burgdorferi*. Infect Immun 71:4711–4716. https://doi.org/10.1128/iai.71.8.4711-4716.2003.
49. Corbin BD, Seeley EH, Raab A, Feldmann J, Miller MR, Torres VJ, Anderson KL, Dattilo BM, Dunman PM, Gerads R, Caprioli RM, Nacken W, Chazin WJ, Skaar EP. 2008. Metal chelation and inhibition of bacterial growth in tissue abscesses. Science 319:962–965. https://doi.org/10.1126/science.1152449.
50. Kapetanovic R, Bokil NJ, Achard MES, Ong C-LY, Peters KM, Stocks CJ, Phan M-D, Monteleone M, Schroder K, Irvine KM, Saunders BM, Walker MJ, Stacey KJ, McEwan AG, Schembri MA, Sweet MJ. 2016. Salmonella employs multiple mechanisms to subvert the TLR-inducible zinc-mediated antimicrobial response of human macrophages. FASEB J 30:1901–1912. https://doi.org/10.1096/fj.201500061.
51. Liu JZ, Jellbauer S, Poe AJ, Ton V, Pesciaroli M, Kehl-Fie TE, Restrepo NA, Hosking MP, Edwards RA, Battistoni A, Pasquali P, Lane TE, Chazin WJ, Vogl T, Roth J, Skaar EP, Raffatellu M. 2012. Zinc sequestration by the neutrophil protein calprotectin enhances Salmonella growth in the inflamed gut. Cell Host Microbe 11:227–239. https://doi.org/10.1016/j.chom.2012.01.017.
52. Peracino B, Wagner C, Balest A, Balbo A, Pergolizzi B, Noegel AA, Steinert M, Bozzaro S. 2006. Function and mechanism of action of *Dictyostelium* Nramp1 (Slc11a1) in bacterial infection. Traffic 7:22–38. https://doi.org/10.1111/j.1600-0854.2005.00356.x.
53. Buracco S, Peracino B, Cinquetti R, Signoretto E, Vollero A, Imperiali F, Castagna M, Bossi E, Bozzaro S. 2015. *Dictyostelium* Nramp1, which is structurally and functionally similar to mammalian DMT1 transporter, mediates phagosomal iron efflux. J Cell Sci 128:3304–3316. https://doi.org/10.1242/jcs.173153.
54. Bozzaro S, Buracco S, Peracino B. 2013. Iron metabolism and resistance to infection by invasive bacteria in the social amoeba *Dictyostelium*

discoideum. Front Cell Infect Microbiol 3:50. https://doi.org/10.3389/fcimb.2013.00050.
55. Knobloch P, Koliwer-Brandl H, Arnold FM, Hanna N, Gonda I, Adenau S, Personnic N, Barisch C, Seeger MA, Soldati T, Hilbi H. 2020. *Mycobacterium marinum* produces distinct mycobactin and carboxymycobactin siderophores to promote growth in broth and phagocytes. Cell Microbiol 22:e13163. https://doi.org/10.1111/cmi.13163.
56. Padilla-Benavides T, Long JE, Raimunda D, Sassetti CM, Argüello JM. 2013. A novel P(1B)-type Mn^{2+}-transporting ATPase is required for secreted protein metallation in mycobacteria. J Biol Chem 288:11334–11347. https://doi.org/10.1074/jbc.M112.448175.
57. Rybniker J, Chen JM, Sala C, Hartkoorn RC, Vocat A, Benjak A, Boy-Röttger S, Zhang M, Székely R, Greff Z, Orfi L, Szabadkai I, Pató J, Kéri G, Cole ST. 2014. Anticytolytic screen identifies inhibitors of mycobacterial virulence protein secretion. Cell Host Microbe 16:538–548. https://doi.org/10.1016/j.chom.2014.09.008.
58. Geertsma ER, Dutzler R. 2011. A versatile and efficient high-throughput cloning tool for structural biology. Biochemistry 50:3272–3278. https://doi.org/10.1021/bi200178z.
59. Arnold FM, Hohl M, Remm S, Koliwer-Brandl H, Adenau S, Chusri S, Sander P, Hilbi H, Seeger MA. 2018. A uniform cloning platform for mycobacterial genetics and protein production. Sci Rep 8:9539. https://doi.org/10.1038/s41598-018-27687-5.
60. Barisch C, Lopez-Jimenez AT, Soldati T. 2015. Live imaging of *Mycobacterium marinum* infection in *Dictyostelium discoideum*. Methods Mol Biol 1285:369–385. https://doi.org/10.1007/978-1-4939-2450-9_23.
61. Qian F, Zhang C, Zhang Y, He W, Gao X, Hu P, Guo Z. 2009. Visible light excitable Zn^{2+} fluorescent sensor derived from an intramolecular charge transfer fluorophore and its in vitro and in vivo application. J Am Chem Soc 131:1460–1468. https://doi.org/10.1021/ja806489y.
62. Ravanel K, de Chassey B, Cornillon S, Benghezal M, Zulianello L, Gebbie L, Letourneur F, Cosson P. 2001. Membrane sorting in the endocytic and phagocytic pathway of *Dictyostelium discoideum*. Eur J Cell Biol 80:754–764. https://doi.org/10.1078/0171-9335-00215.
63. Hanna N, Ouahrani-Bettache S, Drake KL, Adams LG, Köhler S, Occhialini A. 2013. Global Rsh-dependent transcription profile of *Brucella suis* during stringent response unravels adaptation to nutrient starvation and cross-talk with other stress responses. BMC Genomics 14:459. https://doi.org/10.1186/1471-2164-14-459.
64. Arafah S, Kicka S, Trofimov V, Hagedorn M, Andreu N, Wiles S, Robertson B, Soldati T. 2013. Setting up and monitoring an infection of *Dictyostelium discoideum* with mycobacteria. Methods Mol Biol 983:403–417. https://doi.org/10.1007/978-1-62703-302-2_22.
65. Alibaud L, Rombouts Y, Trivelli X, Burguière A, Cirillo SLG, Cirillo JD, Dubremetz J-F, Guérardel Y, Lutfalla G, Kremer L. 2011. A *Mycobacterium marinum* TesA mutant defective for major cell wall-associated lipids is highly attenuated in *Dictyostelium discoideum* and zebrafish embryos. Mol Microbiol 80:919–934. https://doi.org/10.1111/j.1365-2958.2011.07618.x.
66. Kapopoulou A, Lew JM, Cole ST. 2011. The MycoBrowser portal: a comprehensive and manually annotated resource for mycobacterial genomes. Tuberculosis (Edinb) 91:8–13. https://doi.org/10.1016/j.tube.2010.09.006.
67. Katoh K. 2005. MAFFT version 5: improvement in accuracy of multiple sequence alignment. Nucleic Acids Res 33:511–518. https://doi.org/10.1093/nar/gki198.